

Electrostatically Driven Airborne Ultrasound Transducer with Perforated Backplate for Nonlinear Acoustic Applications

Takaaki KAMIGAKI¹; Yuki NINOMIYA²; Hiroyuki SHINODA³

^{1, 2, 3} The University of Tokyo, Japan

ABSTRACT

This paper proposes a capacitive transducer to realize a thin airborne ultrasound phased array for nonlinear acoustic applications. The generation of high-intensity ultrasound requires a displacement of several micrometers of a diaphragm. Conventional capacitive transducers with parallel-plate structure have not achieved this because a thin air layer between the electrodes prevents the diaphragm from vibrating. We have solved the problem by providing perforations at a backplate electrode. The air between the diaphragm and the perforated backplate can travel freely through the perforations when the diaphragm vibrates. We drove the proposed transducer by controlling the amount of electrical charge stored in the diaphragm. This driving method can prevent the pull-in phenomenon. In the experiment, a prototype transducer, with a thickness of 334 μm , emitted 392 Pa (RMS) on the surface when driving at 51 kHz. The diaphragm vibrated with an average amplitude of 3 μm (RMS).

Keywords: Capacitive airborne ultrasound transducer, High-intensity, Perforated backplate

1. INTRODUCTION

High-intensity airborne ultrasound has a diverse range of applications, such as for parametric speaker(1), noncontact tactile display(2–4), air flow control(5), and acoustic manipulation(6–9). Typical devices for the above applications comprise airborne ultrasound phased arrays (AUPAs), using commercial piezoceramic transducers. They can provide arbitrary waveforms with a high temporal resolution by electrically controlling the phase of each transducer. Meanwhile, the existing AUPAs have practical problems, such as their thickness and low efficiency. Solving these problems is necessary for the expansion and practicalization of AUPA applications.

Many thin AUPAs have been developed, such as devices based on piezoelectric transducers(10), capacitive transducers(11), and thermoacoustic transducers(12). However, those piezoelectric and capacitive transducers cannot generate high-intensity airborne ultrasound because they are generally designed for sensing applications. The thermoacoustic transducer can generate high-intensity airborne ultrasound, although its energy efficiency remains to be improved.

The goal of this work is to realize a thin AUPA with high intensity and high efficiency. The target driving frequency is higher than 40 kHz, in reference to the typical piezoceramic transducers. In the previous study, we developed a single capacitive transducer that generates approximately 420 Pa (RMS) at the surface and achieved an electro-acoustic energy conversion efficiency of 55% at 44 kHz when the DC voltage was 500 V and the amplitude of the AC voltage was 150 V(13). This transducer achieved the above characteristics by using a fine mesh electrode knitted with a metal thread as the backplate.

In this paper, we propose a practical structure of the capacitive transducers applicable to the AUPA. The proposed transducer adopts a parallel-plate structure with a perforated backplate. This transducer can be driven with a lower voltage than the mesh electrode type. We experimentally showed that the prototype transducer generated high-intensity airborne ultrasound.

¹ kamigaki@hapis.k.u-tokyo.ac.jp

² ninomiya@hapis.k.u-tokyo.ac.jp

³ hiroyuki_shinoda@k.u-tokyo.ac.jp

2. Problems in Parallel Plate Structure

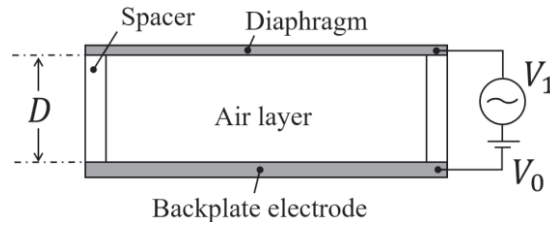


Figure 1 – Typical structure of capacitive transducers.

Figure 1 shows a typical capacitive transducer driven by electrostatic force (ESF) when the AC voltage is applied with the DC voltage. The RMS sound pressure generated from the transducer $|p_0|$ [Pa] is determined by the diaphragm displacement, given by the following equation, assuming that the uniform diaphragm oscillates with a simple harmonic motion:

$$|p_0| = |j\omega\rho c\xi| \quad (1)$$

where ω [rad/s] is the angular frequency, ρ [kg/m³] is the air density, c [m/s] is the acoustic velocity in the air, and ξ [m] is the average RMS displacement of the diaphragm. This equation shows that higher frequencies decrease ξ to obtain the same $|p_0|$. For example, in our measurement, ξ is 5 μm at the 40 kHz piezoceramic transducer (T4010A1, NIPPON CERAMIC CO., LTD.) driven by a sinusoidal voltage with 12 V amplitude, assuming $\rho = 1.2 \text{ kg/m}^3$ and $c = 340 \text{ m/s}$. To obtain the same intensity at 80 kHz, ξ is 2.5 μm . The existing parallel-plate transducers have not achieved the above displacement due to the three factors described below.

2.1 Discharge between Electrodes

Increasing the electric field intensity (EFI) between the diaphragm and the backplate electrode contributes to increasing the diaphragm displacement because the ESF increases with the proportional square of the EFI. The applied voltage is limited to a discharge voltage decided by the air gap D [m] and the internal pressure p_{in} [Pa]. The discharge voltage in the parallel-plate structure V_B [V] is obtained by Paschen's law, given by:

$$V_B = \frac{Bp_{in}D}{\ln(Ap_{in}D) - \ln\ln\left(\frac{1}{1+\gamma}\right)} \quad (2)$$

where A and B [(Pa \cdot m)⁻¹] are constants determined by the gas between the electrodes, and γ [-] is the number of electrons emitted from a cathode by γ -action. Figure 2(a) shows the numerical calculation results of V_B and the EFI against D based on Eq. (2). This figure shows that the increase of the EFI without discharge can be achieved by shortening D .

2.2 Viscosity Loss in Air Layer

The loss in the structure should be as small as possible compared with the radiated power to obtain high efficiency. The decrement of D enables a higher driving force, according to Fig. 2(a). However, extremely shorting D in the airtight structure, as shown in Fig. 1, increases the inevitable loss in the structure due to viscosity in the air layer. The thermal conduction loss also contributes to the efficiency, but it is minor compared with the viscosity loss. Figure 2(b) shows our numerical calculation result of the electro-acoustic conversion efficiency, considering the air viscosity and thermal conduction. This graph shows that increasing D contributes to higher efficiency, which is a trade-off against increasing the EFI.

2.3 Pull-in Phenomenon

The pull-in phenomenon is a well-known problem with the parallel-plate structure. The diaphragm becomes immobile by sticking to the backplate when a predetermined voltage is applied between the electrodes. To avoid pull-in, it is necessary to apply the voltage within the range where the diaphragm displacement does not exceed $D/3$. The cause of this phenomenon is the collapse of the force balance acting on the diaphragm, i.e., the ESF becomes larger than a restoring force due to the diaphragm stiffness.

Capacitive transducers using the pull-in phenomenon have been proposed(14,15). These methods

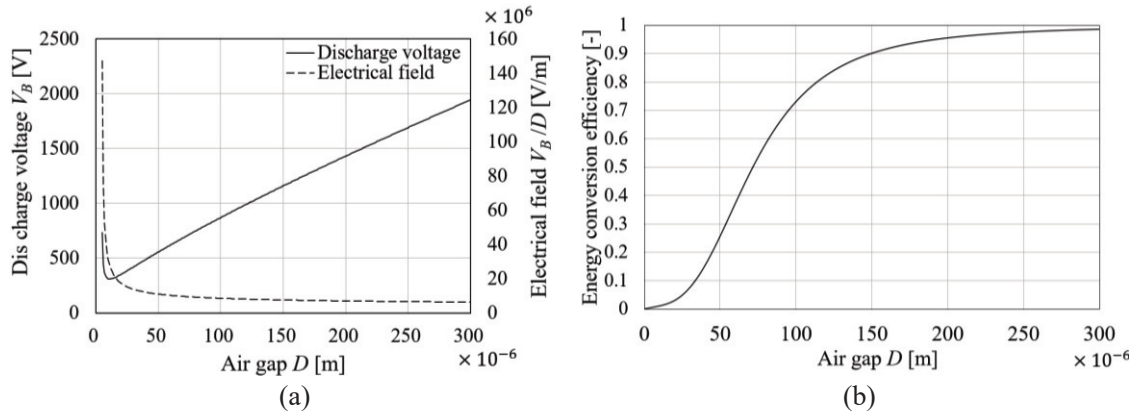


Figure 2 – Numerical calculation results of: (a) discharge voltage V_B and its electric field against the air gap D , and (b) energy efficiency of the parallel-plate structure against D .

can generate a higher sound pressure than those without pull-in, but their sound pressure is outside the scope of the target sound pressure.

3. Proposed Transducer

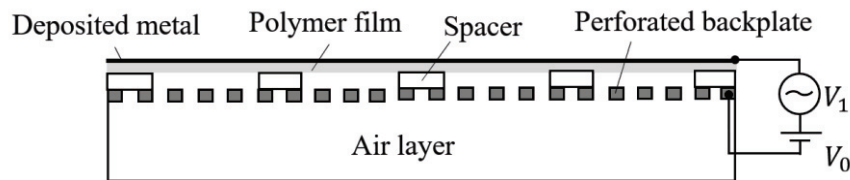


Figure 3 – Cross-sectional view of a proposed structure with a perforated backplate electrode.

Figure 3 shows the proposed structure of a single transducer to solve the problems. The proposed structure is realized by arranging periodically repeated spacers in one direction between a series of a diaphragm and a perforated backplate electrode. The air gap between the diaphragm and the backplate is set to $10 \mu\text{m}$ to secure the diaphragm displacement, assuming that the driving frequency is higher than 40 kHz, as mentioned in Section 2. This distance supplies a high EFI. The air between the diaphragm and the backplate can travel freely through the perforations when the diaphragm vibrates. Therefore, the proposed structure can increase the driving force with suppression of the viscosity loss.

To ensure the diaphragm displacement without the pull-in, we propose a driving method by controlling the charge amount. The proposed method repeats storage and dissipation in the structure every half of the driving cycle. The stored and dissipation time is sufficiently short, compared with half of the driving cycle. The ESF is constant regardless of the electrode distance because the stored electrical charge is constant. Thus, the diaphragm can be attracted towards the backplate without the pull-in. When the electrical charge is dissipated, the diaphragm lifts the outside air by diaphragm stiffness. The push-pull circuit realizes the driving method.

Many capacitive transducers with a perforated backplate have been proposed. However, they are not suitable for generating high-intensity ultrasound because their air gap is typically shorter than $1 \mu\text{m}$.

4. Experiments

4.1 Prototype Transducers

Figure 4 shows the prototype transducer by laminating the diaphragm on a stainless structure. The diaphragm was a $4.4\text{-}\mu\text{m}$ -thick aramid film (Mictron, TORAY INDUSTRIES, INC.) deposited with 30-nm-thick platinum. The stainless structure comprises three stainless steel plates of different thicknesses (SHIN-EI SANGYO CO., LTD). The top and bottom layers were spacers, and their

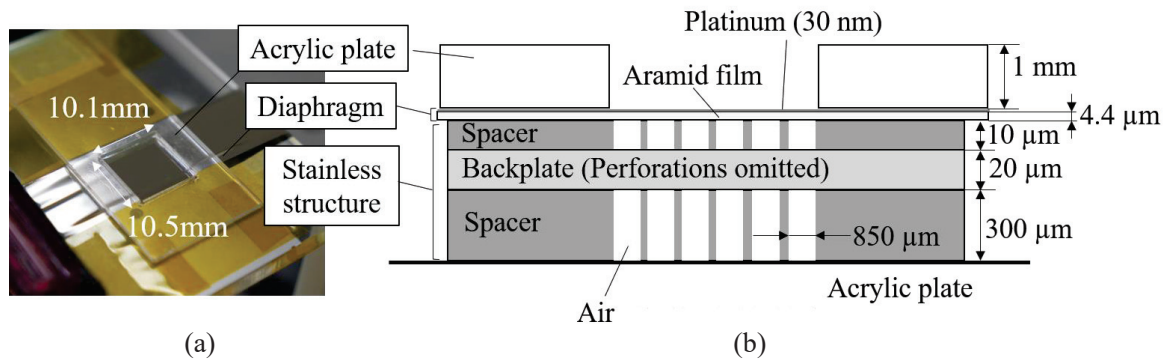


Figure 4 – (a) Photograph of a prototype transducer; (b) Cross-sectional view of the prototype transducer.

thicknesses were $10\ \mu\text{m}$ and $300\ \mu\text{m}$, respectively. The spacer width was $150\ \mu\text{m}$ with the interval to the next spacer was $850\ \mu\text{m}$. The middle layer was a $20\text{-}\mu\text{m}$ -thick perforated backplate. The backplate had repeated rectangular openings of $80\ \mu\text{m} \times 500\ \mu\text{m}$. We selected the dimensions after theoretical consideration in reference to (16, 17) because they contribute to the air viscosity loss.

The total movable area of the diaphragm was $10.1\ \text{mm} \times 10.5\ \text{mm}$. We minimized the peripheral area where the diaphragm and stainless structure overlap out of the movable area. Furthermore, we covered the peripheral area by placing a 1-mm -thick acrylic plate with a $10.1\ \text{mm} \times 10.5\ \text{mm}$ aperture on the prototype surface so that sound waves from the peripheral area do not affect the measurement sound pressure. We inserted a $12.5\text{-}\mu\text{m}$ -thick insulating film (Kapton 50EN, DU PONT-TORAY INDUSTRIES, INC.) between the diaphragm and the stainless structure to prevent discharge.

We fabricated two kinds of transducers to obtain the contribution of the diaphragm stiffness to the generated sound pressure. One type is the diaphragm with applied external tension in one direction. The other type is the diaphragm without external tension. The value of the external tension was not quantified because the tension was applied by the author's hand. We fabricated two transducers of each type.

4.2 Experimental Results

We measured the generated sound pressure within the applied voltage range where no discharge occurs. A standard microphone (4138-A015, Bruel&Kjaer) was set $20\ \text{cm}$ above the transducer and the sound pressure was obtained by an oscilloscope (DCS-1074B, TEXIO CORPORATION) connected to the microphone through an amplifier (NEXUS Conditioning Amplifier, Bruel&Kjaer). We confirmed that interference is negligible by measuring the sound pressure fluctuations when the microphone was moved from the original position. The push-pull circuit was used to drive the prototype transducer. The storage and dissipation time was one-eighth of the driving cycle.

First, we obtained the frequency characteristics of each transducer. The applied voltage for the transducer was $100\ \text{V}$ when the diaphragm was at the initial gap. Figure 5 shows the frequency characteristics of the four prototype transducers. The RMS sound pressure $|p|$ observed at $20\ \text{cm}$ above each prototype transducer was calculated by Fourier transformation. The result shows a peak at $51\ \text{kHz}$ when the diaphragm was with applied external tension, and the peaks around $86\ \text{kHz}$ exist regardless of the external tension.

Next, we obtained the contribution of the applied voltage to the generated sound pressure at the peak frequency of both types (V_2 in Fig. 5), i.e., $60\ \text{kHz}$ and $88\ \text{kHz}$ in the case without the external tension, and $51\ \text{kHz}$ and $86\ \text{kHz}$ in the case with the external tension. The experimental setup was the same as the first experiment. The applied voltage was from $50\ \text{V}$ to $300\ \text{V}$ when the diaphragm was at the initial gap. Figure 6(a) shows the RMS sound pressure $|p|$ observed at $20\ \text{cm}$ above each prototype transducer and Fig. 6(b) shows the calculated RMS sound pressure at the prototype surface $|p_0|$, following the theoretical relationship between the device surface pressure and pressure in the air (18). The maximum $|p_0|$ was $392\ \text{Pa}$ at $51\ \text{kHz}$ when the maximum voltage was applied to the transducer. In this time, the average displacement of the diaphragm was approximately $3\ \mu\text{m}$, as calculated using Eq. (1).

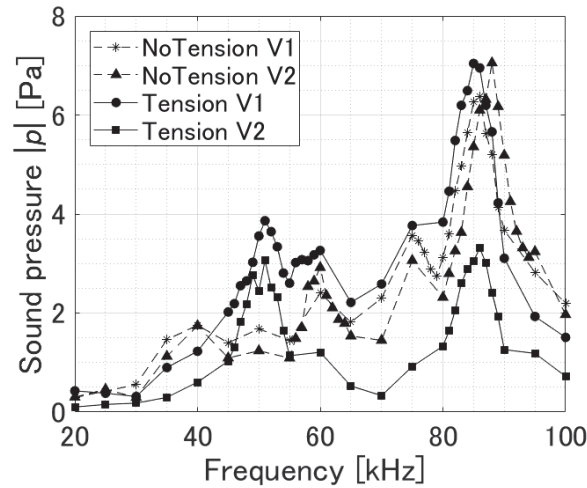


Figure 5 – Frequency characteristic of each prototype transducer. The sound pressure was obtained at 20 cm.

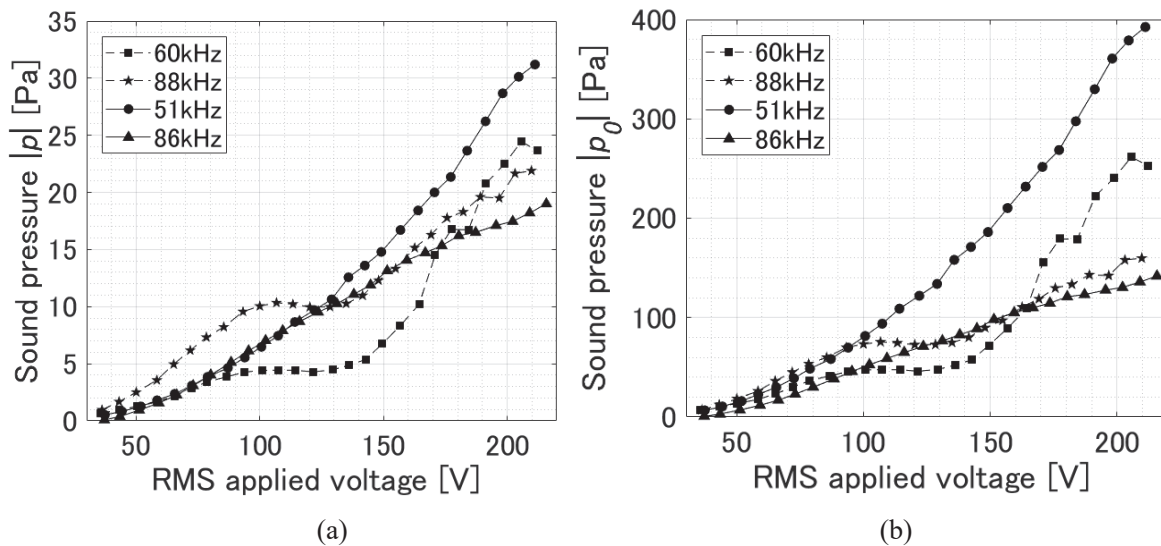


Figure 6 – Applied voltage contribution to generated sound pressure. (a) Sound pressure obtained at 20 cm, (b) sound pressure at prototype surface.

4.3 Discussion

In the first experiment, the peaks occur at around 86 kHz regardless of the external tension state. It is assumed this is due to the resonance of the perforated backplate. We analyzed the resonant frequency of the backplate supported by the spacers, using ANSYS 19.1(ANSYS Inc.), and confirmed that the resonant frequency was 83 kHz. In the second experiment, the generated sound pressure at 51 kHz increased proportional to the approximate square of the applied voltage according to the principle, whereas the other did not increase according to the principle. This reason is not obvious, and the dynamic mechanism in the large-amplitude operation is still unclear.

5. Conclusions

In this paper, we proposed a practical capacitive transducer for AUPA. The proposed transducer, with a perforated backplate, enhanced the ESF with the suppression of the viscosity loss. The transducer emits airborne ultrasound by controlling the amount of electrical charge accumulated in the diaphragm. In the experiment, we obtained 392 Pa (RMS) at 51 kHz. In the future, we will measure the electro-acoustic energy efficiency and clarify the mechanism.

ACKNOWLEDGEMENTS

This research was supported by JSPS KAKENHI Grant Number JP16H06303 and JST CREST JPMJCR18A2.

REFERENCES

1. Yoneyama M, Fujimoto J, Kawamo Y, Sasabe S. The audio spotlight: An application of nonlinear interaction of sound waves to a new type of loudspeaker design. *J Acoust Soc Am*. 1983;73(5):1532–1536.
2. Iwamoto T, Tatzono M, Shinoda H. Non-contact method for producing tactile sensation using airborne ultrasound. In: *International conference on human haptic sensing and touch enabled computer applications*. Springer; 2008. p. 504–513.
3. Hoshi T, Takahashi M, Iwamoto T, Shinoda H. Noncontact tactile display based on radiation pressure of airborne ultrasound. *IEEE Trans Haptics*. 2010;3(3):155–165.
4. Carter T, Seah SA, Long B, Drinkwater B, Subramanian S. UltraHaptics: multi-point mid-air haptic feedback for touch surfaces. In: *Proceedings of the 26th annual ACM symposium on User interface software and technology*. ACM; 2013. p. 505–514.
5. Hasegawa K, Qiu L, Noda A, Inoue S, Shinoda H. Electronically steerable ultrasound-driven long narrow air stream. *Appl Phys Lett*. 2017;111(6):064104.
6. Ochiai Y, Hoshi T, Rekimoto J. Pixie dust: graphics generated by levitated and animated objects in computational acoustic-potential field. *ACM Trans Graph TOG*. 2014;33(4):85.
7. Inoue S, Mogami S, Ichiyama T, Noda A, Makino Y, Shinoda H. Acoustical boundary hologram for macroscopic rigid-body levitation. *J Acoust Soc Am*. 2019;145(1):328–337.
8. Marzo A, Seah SA, Drinkwater BW, Sahoo DR, Long B, Subramanian S. Holographic acoustic elements for manipulation of levitated objects. *Nat Commun*. 2015;6:8661.
9. Furumoto T, Hasegawa K, Makino Y, Shinoda H. Three-dimensional manipulation of a spherical object using ultrasound plane waves. *IEEE Robot Autom Lett*. 2019;4(1):81–88.
10. Kato Y, Sekitani T, Noguchi Y, Yokota T, Takamiya M, Sakurai T, et al. Large-area flexible ultrasonic imaging system with an organic transistor active matrix. *IEEE Trans Electron Devices*. 2010;57(5):995–1002.
11. Haller MI, Khuri-Yakub BT. A surface micromachined electrostatic ultrasonic air transducer. *IEEE Trans Ultrason Ferroelectr Freq Control*. 1996;43(1):1–6.
12. Shinoda H, Nakajima T, Ueno K, Koshida N. Thermally induced ultrasonic emission from porous silicon. *Nature*. 1999;400(6747):853.
13. Kamigaki T, Ninomiya Y, Shinoda H. Electrostatically driven airborne ultrasound transmitter with fine mesh electrode. In: *2018 International flexible electronics technology conference (IFETC)*. IEEE; 2018. p. 1–3.
14. Oralkan O, Bayram B, Yaralioglu GG, Ergun AS, Kupnik M, Yeh DT, et al. Experimental characterization of collapse-mode CMUT operation. *IEEE Trans Ultrason Ferroelectr Freq Control*. 2006;53(8):1513–1523.

15. Olcum S, Yamaner FY, Bozkurt A, Atalar A. Deep-collapse operation of capacitive micromachined ultrasonic transducers. *IEEE Trans Ultrason Ferroelectr Freq Control*. 2011;58(11):2475–2483.
16. Škvor Z. On the acoustical resistance due to viscous losses in the air gap of electrostatic transducers. *Acta Acust United Acust*. 1967;19(5):295–299.
17. Hayasaka T, Yoshikawa S. *Onkyo shindouron*. Maruzen. 1974. p. 702–703.
18. Hayasaka T, Yoshikawa S. *Onkyo shindouron*. Maruzen. 1974. p. 612–616.